Macromolecules

ARTICLE

pubs.acs.org/Macromolecules

Phase Behavior and Ionic Conductivity of Lithium Perchlorate-Doped Polystyrene-*b*-poly(2-vinylpyridine) Copolymer

Sudhakar Naidu, Hyungju Ahn, Jinsam Gong, Bokyung Kim, and Du Yeol Ryu*

Department of Chemical and Biomolecular Engineering, Yonsei University, Seoul 120-749, Korea

Supporting Information

ABSTRACT: The phase transitions of lithium perchlorate ($LiClO_4$)-doped polystyrene-*b*-poly(2-vinylpyridine) (PS-*b*-P2VP) were studied as a function of temperature and ion salt concentration using *in situ* small-angle X-ray scattering (SAXS) and transmission electron microscopy (TEM). Incorporation of $LiClO_4$ into an asymmetric, disordered PS-*b*-P2VP copolymer produced temperature-dependent order−disorder (ODT) and order−order transitions (OOTs) from spherical to lamellar microphases. The effective interaction parameter (χ_{eff}) between two block components was evaluated for low molecular weight $LiClO_4$-doped PS-*b*-P2VP in a disordered state. With increasing quantities of $LiClO_4$, a remarkable increase in χ along with a volumetric change produced by the selective coordination of $LiClO_4$ to the ionophilic P2VP block led to morphological transitions from disordered (DIS) to body-centered cubic spherical (BCC) to hexagonally packed cylindrical (HEX) to lamellar (LAM) structures. We also demonstrate that the ionic conductivity in the samples quenched from the different structures is morphology-independent, while it increases with increasing salt concentration.

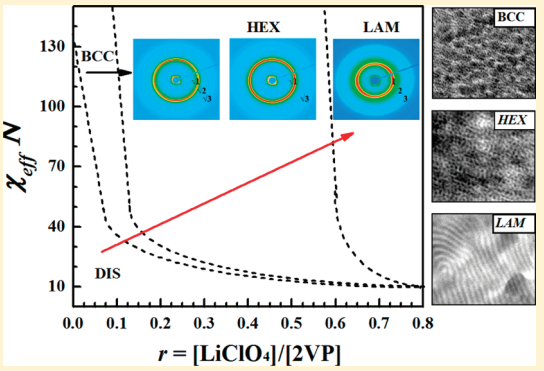

INTRODUCTION

Ion-doped polymers have recently received attention as promising ion-conductive soft materials for applications in electrochemical devices such as rechargeable lithium batteries, fuel cells, and dye-sensitized solar cells.[1−18] These materials offer advantages for both manufacturing and safety; in particular, they are easily processed and nonflammable. Solid-state polymer electrolytes are produced via the coordination or complex formation of alkaline metal salts in a host polymer, which enhances the ionic conductivity of the miscible phase.[19,20] Some research efforts have been directed toward block copolymer (BCP) self-assembly with the goal of a desirable performance between the ionic conductivity and the mechanical stability, since an ion-doped BCP self-assembly both resists deformation and facilitates ionic transport through the periodic nanostructured arrays.[13−15,21−27]

Generally, a diblock copolymer composed of two chemically different, covalently bonded polymers can self-assemble into ordered arrays with nanostructures such as lamellar (LAM), hexagonally packed cylindrical (HEX), gyroid (GYR), body-centered cubic spherical (BCC), and hexagonally perforated layers (HPL) microdomains.[28−32] When the Flory−Huggins interaction parameter (χ) between two block components is inversely proportional to temperature (or χ decreases with increasing temperature), a phase diagram for a BCP can be dictated by the product of χN as a function of the volume fraction of one component, where N is the overall number of segments.[31−37] In the case of a symmetric BCP of $\chi N > 10.495$, microphase separation occurs, while a phase-mixed or disordered state can be observed when $\chi N < 10.495$ in the weak segregation regime.[37] Therefore, when mixing between two block components occurs at a thermodynamically balanced state in the free energy, order−disorder transition (ODT) and order−order transition (OOT) behavior of BCPs can be measured with increasing temperature up to the disordered (or physically phase-mixed) state.[32,38] Pertinent studies on the effects of ion doping in BCP melts describe an increase in the ODT, resulting from the selective coordination of ion salts to the ionophilic block component. These results were found to be valid for copolymers with salt-compatible components such as poly(ethylene oxide) (PEO) derivatives,[2−4,24,39−41] poly(methyl methacrylate) (PMMA),[13,14,42] and poly(vinylpyridine) (PVP),[24,43,44] indicating that the presence of ion salts influences the size of the microphases and transition behavior in ion-doped BCPs.

An intriguing question is whether the ionic conductivity is influenced by transition behavior for ion-doped BCPs such as ODTs and OOTs. Despite its importance, however, there are only a few reports on this issue. Mayes et al. reported a deviation from the Vogel−Tamman−Fulcher (VTF) equation at the ODT (rather than a discontinuity) in lithium trifluoromethanesulfonate ($LiCF_3SO_3$)-doped poly(methyl methacrylate)-*b*-poly(oligo oxyethylenemethacrylate) (PMMA-*b*-POEM).[13] Wiesner et al. showed distinct discontinuous changes in the ionic conductivity at OOTs in $LiCF_3SO_3$-doped amphiphilic

Received: February 23, 2011
Revised: June 17, 2011
Published: July 13, 2011

Table 1. Molecular Composition and Transition for $LiClO_4$-Doped PS-*b*-P2VP-30s

molar ratio (r)[a]	W_P[b]	W_S (f_S)[c]	transitions
0	1	0.844 (0.854)	DIS
0.03	0.995	0.840	DIS
0.06	0.991	0.836	BCC-DIS
0.09	0.986	0.832	BCC-DIS
0.12	0.981	0.828	HEX-BCC
0.15	0.977	0.824	HEX-BCC
0.2	0.969	0.818	HEX-BCC
0.3	0.955	0.806	HEX
0.39	0.942	0.795	HEX
0.51	0.925	0.781	HEX
0.61	0.912	0.770	LAM-HEX

[a] The molar ratio (r) = [$LiClO_4$]/[2VP]. [b] W_P denotes the weight fraction of block copolymer. [c] The weight (W_S) and volume (f_S) fractions of PS block component were evaluated by ^{1}H nuclear magnetic resonance (NMR) with mass densities of components (1.05, 1.14, and 2.42 g/cm^3 for PS, P2VP, and $LiClO_4$, respectively).

dendrons with PEO.[2] In contrast, Balsara et al. reported that a phase transition has no effect on the ionic conductivity in lithium bis(trifluoromethylsulfonimide) (LiTFSI)-doped polystyrene-*b*-poly(ethylene oxide) (PS-*b*-PEO).[39] In addition, Winey and Elabd observed that an alignment (or orientation) of microdomains significantly enhances the ionic conductivity in BCP mixtures with ionic liquids.[45]

Previously, we observed the transition behavior of lithium perchlorate ($LiClO_4$) doped polystyrene-*b*-poly(2-vinylpyridine) (PS-*b*-P2VP) on the basis of ODT changes within a lamellar morphology, where selective ionic coordination is available at the nitrogen units of the P2VP block.[43] In the present study, we extensively examined the phase transition behavior for $LiClO_4$-doped PS-*b*-P2VP for morphologies from disordered to lamellar. Incorporation of $LiClO_4$ into an asymmetric, disordered PS-*b*-P2VP copolymer produced ODTs, OOTs, and a variety of microphases including BCC, HEX, and LAM, which can be attributed to an increase in χ between two block components as well as to a volumetric change produced by the selective coordination of $LiClO_4$ to the ionophilic P2VP block. Especially in the samples quenched from the different structures, we demonstrate that the ionic conductivity is morphology-independent, while it increases with increasing ion salt concentration.

EXPERIMENTAL SECTION

Materials. The two polystyrene-*b*-poly(2-vinylpyridine)s (PS-*b*-P2VPs) used in this study were synthesized by the sequential, anionic polymerization of styrene and 2-vinylpyridine in tetrahydrofuran (THF) at −78 °C in a purified argon environment using *sec*-butyllithium as an initiator. Refluxed THF from CaH_2 was stirred over fresh sodium-benzophenone complex until it showed a deep purple color, indicating an oxygen- and moisture-free solvent.[43] Degassed monomers with CaH_2, styrene and 2-vinylpyridine (Aldrich), were vacuum distilled over dried dibutyl magnesium and trioctyl aluminum, respectively, until a persistent, characteristic color was observed. The polymer solution terminated with purified 2-propanol was precipitated in excess hexane. The absolute weight-average and number-average molecular weights (M_w and M_n) and polydispersity (M_w/M_n) were measured by size-exclusion chromatography (SEC) on the basis of terminated PS block with PS standards. The PS volume fraction (f_{PS}) of PS-*b*-P2VPs was determined by ^{1}H nuclear magnetic resonance (^{1}H NMR) with mass densities of the two components (1.05 and 1.14 g/cm^2 for PS and P2VP, respectively). PS-*b*-P2VP-18 with M_n = 17500 g/mol (f_{PS} = 0.862) was used to obtain the effective interaction parameter (χ_{eff}) between two block components, and PS-*b*-P2VP-30 with M_n = 30000 g/mol (f_{PS} = 0.854) was used for phase transition and the ionic conductivity experiments. SEC results for both PS-*b*-P2VPs indicate a quite narrow distribution (M_w/M_n< 1.06). The lithium perchlorate ($LiClO_4$) was dried at 120 °C for 12 h under vacuum prior to all the experiments, because it is highly hygroscopic.

PS-*b*-P2VPs with various amounts of $LiClO_4$ were prepared by freeze-drying from benzene solution. Predetermined amounts of PS-*b*-P2VP and $LiClO_4$ were dissolved in benzene (~8 wt % in solution) and ethanol, respectively, and the quenched solution was evaporated under vacuum for 24 h, followed by sequential annealing at 170 °C for 3 days to thermally equilibrate the sample and to remove remaining solvent. The molar ratio of $LiClO_4$ to 2-vinylpyridine (2VP) in PS-*b*-P2VP, denoted as r = [$LiClO_4$]/[2VP], was varied up to approximately 0.6, as listed in Table 1.

Small-Angle X-ray Scattering (SAXS). To observe the phase transitions of $LiClO_4$-doped PS-*b*-P2VPs, synchrotron SAXS measurements were conducted in the 4C1 beamline at Pohang Light Source (PLS), Korea. All samples were pressed into disk form (with a thickness of 1.5 mm) by manual compression molding at 160 °C. This helps to avoid scattering at lower q that arises from the presence of bubbles. The SAXS operating conditions were set as follows: wavelength of 1.608 Å ($\Delta\lambda/\lambda = 1.5 \times 10^{-2}$), sample-to-detector distance of 3 m, and beam size of 1 × 1 mm^2. A 2D-CCD detector (Princeton Instruments Ins., SCX-TE/CCD-1242) was used to collect the scattered X-rays. A custom-built heating cell was used for temperature sweep experiments under nitrogen flow to avoid thermal degradation of the polymer samples. The *in situ* scattering profiles were collected with an exposure time of 60−120 s. A polyethylene (PE) standard sample was used to calibrate the absolute intensity for $LiClO_4$-doped PS-*b*-P2VPs.

Transmission Electron Microscopy (TEM). Electron microscopy was used to confirm the morphologies for $LiClO_4$-doped PS-*b*-P2VPs. The samples annealed at various temperatures were quenched in liquid nitrogen to freeze the morphology. The TEM (S-7600, Hitachi)) was operated at an accelerating voltage of 120 kV. Ultrathin specimens were prepared using an ultramicrotome (RMC MT-7000) with a diamond knife at room temperature. The specimens were selectively stained with iodine for ~2 h at room temperature to enhance the contrast between the two phases.

Conductivity Measurement. The ionic conductivity (σ) of $LiClO_4$-doped PS-*b*-P2VP-30 was measured by an ac impedance analyzer (IM6e, ZAHNER, Germany) using a lab-made four-probe Teflon cell-equipped with a temperature controller, where operating frequency ranges from 1 MHz to 1 Hz in galvanostatic mode with an AC current amplitude of 0.01 mA. σ (S/cm) is calculated by $\sigma = L/R \times S$, where L (in cm), R (in Ω), and S (in cm^2) are the distance between the electrodes, the impedance, and the surface area for ions to penetrate the polymer electrolyte, respectively. The samples were annealed at target temperatures under vacuum for 3 days, and then pressed into disk form (with thickness of 1.0 mm) at the same temperatures, followed by quenching them in liquid nitrogen (−196 °C). All the samples were stored under vacuum before measurements to avoid moisture ingress.

RESULTS AND DISCUSSION

The SAXS intensity profiles for asymmetric PS-*b*-P2VP-30 (f_{PS} = 0.854) in the bulk state are shown in Figure 1 as a function of the scattering vector (q), where $q = (4\pi/\lambda)\sin\theta$; here, 2θ and λ are the scattering angle and wavelength, respectively. All the

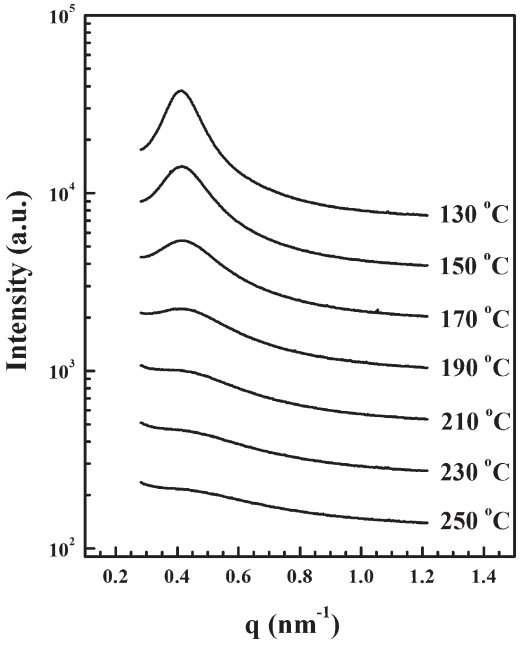

Figure 1. SAXS intensity profiles for PS-*b*-P2VP-30 as a function of scattering vector (q). All the profiles were measured at various temperatures during heating from 130 to 250 °C, well above the glass transition temperatures of PS (100 °C) and P2VP (107 °C). The intensity profiles are vertically shifted by a factor of 2 for clarity.

profiles were measured at various temperatures during heating from 130 to 250 °C, well above the glass transition temperatures of PS (100 °C) and P2VP (107 °C).[46] At a low temperature (130 °C), a broad maximum near $q^* = 0.412$ nm^{-1} corresponds to the characteristic correlation hole scattering of the disordered (or phase-mixed) BCP melt, which can be correlated to the compositional fluctuations in the R_g (radius of gyration) length scale. Even this primary peak appreciably weakens and broadens as temperature increases, indicating a typical ODT-type behavior where the Flory−Huggins interaction parameter (χ) between two block components is inversely proportional to temperature (or χ decreases with increasing temperature). Depolarized light scattering (DPLS) measurements also confirm a disordered state over the entire temperature range studied (data shown in the Supporting Information).

The molar ratio of $LiClO_4$ to 2-vinylpyridine (2VP) in PS-*b*-P2VP-30 (denoted as r = [$LiClO_4$]/[2VP]) was varied to observe the effect of ion salt concentration on phase behavior. Figure 2a shows the SAXS intensity profiles for PS-*b*-P2VP-30 at $r = 0.06$, which were measured at various temperatures during heating from 150 to 250 °C at a rate of 1 °C/min. At low temperatures (T < 207 °C), a sharp scattering peak located at $q^* = 0.359$ nm^{-1} indicates an increase in r (or amount of $LiClO_4$ to disordered PS-*b*-P2VP-30) leads to microphase separation. The primary peak at q^* and the higher-order peaks at $\sqrt{2}q^*$ and $\sqrt{3}q^*$ relative to the first-order reflection are characteristic of body-centered cubic spherical (BCC) microdomains. The BCC morphology was confirmed with a transmission electron microscopy (TEM) image, obtained by quenching the sample at 170 °C, as shown in the inset of Figure 2a. As the P2VP block was selectively stained with iodine, the image indicates the dark periodic P2VP-rich spheres in the bright PS matrix. With further increases in temperature (T > 207 °C), the primary peak significantly

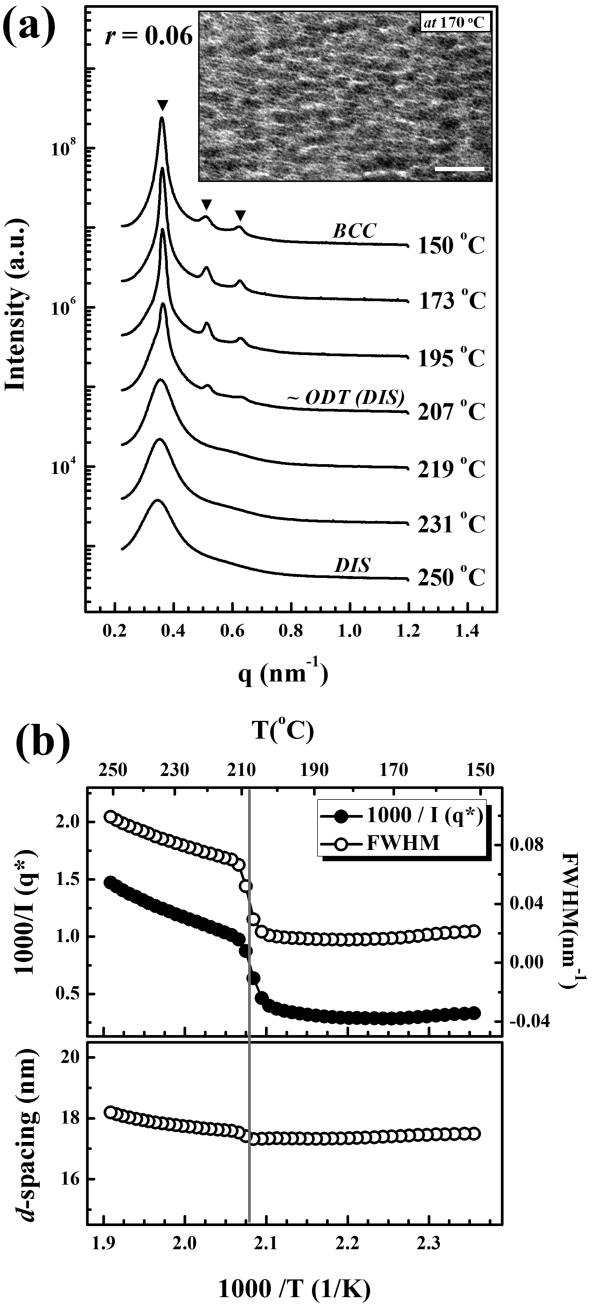

Figure 2. (a) SAXS intensity profiles for PS-*b*-P2VP-30 at $r = 0.06$ as a function of the scattering vector (q). All the profiles were measured at various temperatures during heating at a rate of 1 °C/min from 150 to 250 °C. The intensity profiles are vertically shifted by a factor of 5 for clarity. The TEM image in inset was obtained by quenching the sample at 170 °C, indicating a BCC microdomain. The scale bar indicates 100 nm. (b) Inverse of the maximum intensity ($1/I(q^*)$), full-width at half-maximum (fwhm), and d-spacing ($d = 2\pi/q^*$) as a function of inverse temperature (1/K).

weakens and broadens, and then maintains a broad maximum due to the disordered (DIS) state of $LiClO_4$-doped PS-*b*-P2VP. To reasonably determine the transition temperature, the scattering parameters derived from the SAXS profiles such as the inverse of the maximum intensity ($1/I(q^*)$), full-width at half-maximum (fwhm), and d-spacing ($d = 2\pi/q^*$) are plotted in Figure 2b as a function of inverse temperature (1/K). One can readily

dx.doi.org/10.1021/ma200429v |*Macromolecules* 2011, 44, 6085–6093

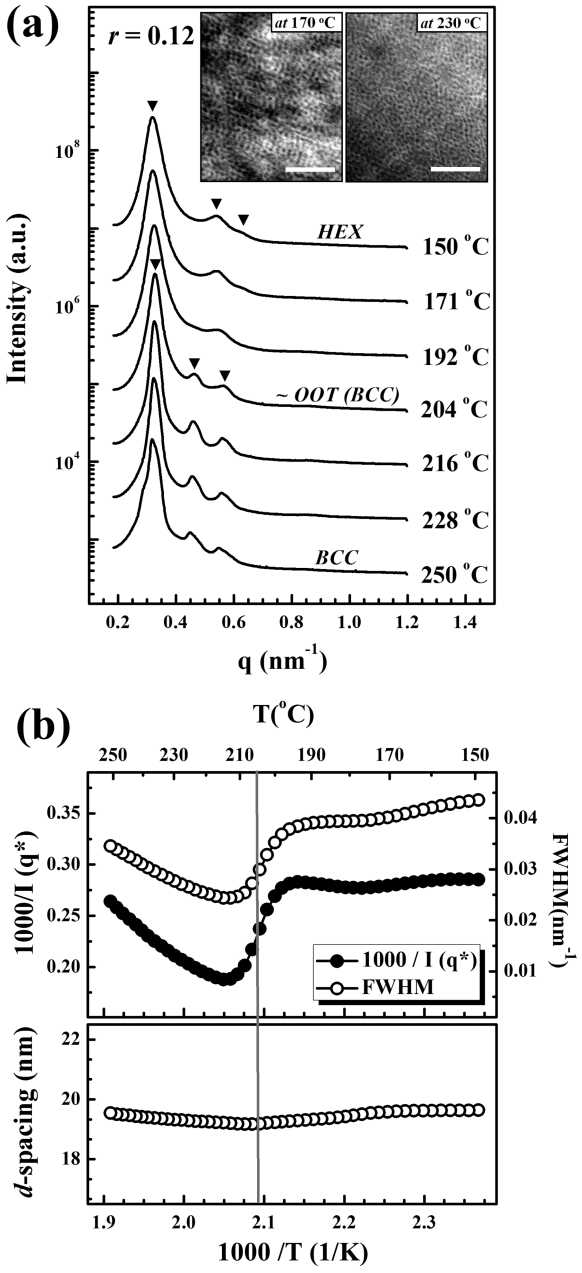

Figure 3. (a) SAXS intensity profiles for PS-*b*-P2VP-30 at $r = 0.12$ as a function of the scattering vector (q). All the profiles were measured at various temperatures during heating at a rate of 1 °C/min from 150 to 250 °C. The intensity profiles are vertically shifted by a factor of 5 for clarity. The TEM images in inset were obtained by quenching the sample at 170 and 230 °C, indicating HEX and BCC microdomains, respectively. The scale bar indicates 100 nm. (b) The inverse of the maximum intensity ($1/I(q^*)$), full-width at half-maximum (fwhm), and *d*-spacing ($d = 2\pi/q^*$) as a function of inverse temperature (1/K).

determine an ODT at 207 °C by a discontinuous change in the scattering parameters.

An increase in *d*-spacing above the ODT with increasing temperature is noteworthy. We speculate that the dominant molecular interactions are the repulsive interactions between two block components in BCC-to-DIS regime of low ion salt concentration, rather than the coordinative interaction of the polymer with $LiClO_4$. Hence, the observed behavior of asymmetric BCPs forming a BCC structure would not be surprising, because it is similar to the behavior observed in a liquid-like short-range order (LSO) regime for asymmetric polystyrene-*b*-poly(ethylene-*co*-but-1-ene)-*b*-polystyrene (SEBS).[47] This is in contrast to the disordering process in LAM and HEX microdomains, where *d*-spacing decreases with increasing temperature. A similar transition from BCC to DIS was observed at $r = 0.03$ and 0.09, while the ODT increases with increasing r (or amount of $LiClO_4$).

Figure 3a, as a representative of the hexagonally packed cylindrical (HEX) to BCC transitions, shows the SAXS intensity profiles for PS-*b*-P2VP-30 at $r = 0.12$, measured during heating from 150 to 250 °C at a rate of 1 °C/min. At low temperatures ($T \leq$ 192 °C), a primary scattering peak located at $q^* = 0.319$ nm^{-1} and the higher-order peaks at $\sqrt{3}q^*$ and $\sqrt{4}q^*$ relative to the first-order reflection indicate HEX microdomains. At $T = 204$ °C, the primary peak at q^* becomes sharper and more intense. At $T \geq$ 204 °C, the sample exhibits BCC microdomains with peaks at $q^* = 0.323$ nm^{-1}, $\sqrt{2}q^*$ and $\sqrt{3}q^*$ relative to the first-order reflection. Therefore, an OOT from HEX to BCC microdomains was determined at 204 °C from the discontinuous change in $1/I(q^*)$ and fwhm. This is confirmed in the inset TEM images (obtained by quenching the sample at 170 and 230 °C), where the dark P2VP-rich phase is stained in the bright PS matrix. A similar transition from HEX to BCC was observed at $r = 0.15$ and 0.20, while the OOT increases with increasing r. A small shoulder (or asymmetry) near the primary peak at $T = 250$ °C might be attributed to an imperfection in BCC structure at higher temperature though minor. The *d*-spacing in HEX-to-BCC regime at $r = 0.12$ appears to be less temperature-dependent, more than likely because with increasing temperature a volumetric increase arising from a weakening of the coordinative interaction with $LiClO_4$ is somehow balanced with a volumetric decrease associated with a decrease in χ between two block components.

Further increasing molar ratio of $LiClO_4$ to disordered PS-*b*-P2VP-30 to $r = 0.61$ results in LAM-to-HEX transition with increasing temperature, as shown in Figure 4a. The SAXS intensity profiles at lower temperatures ($T \leq 191$ °C) indicate LAM microdomains with peaks at $q^* = 0.193$ nm^{-1}, $2q^*$, $3q^*$, and $4q^*$ relative to the first-order reflection. Even though slight asymmetry in the primary peak is also seen, presumably due to an imperfection in the structure, the inset TEM image (obtained by quenching the sample at 180 °C) distinctly exhibits a typical LAM microdomain with the dark P2VP-rich and the bright PS lamellae. At $T \geq 203$ °C, a significant shift in the primary peak toward higher q and the corresponding peaks at $q^* = 0.211$ nm^{-1}, $\sqrt{3}q^*$, and $\sqrt{7}q^*$ relative to the first-order reflection indicate a LAM-to-HEX transition. It was confirmed that the OOT from LAM to HEX microdomains occurs at 203 °C by the discontinuous change in $1/I(q^*)$, fwhm, and *d*-spacing. It appears that the higher molar ratio of $LiClO_4$ to PS-*b*-P2VP-30, the broader the transition temperature is, since polymer chain mobility is restricted by the selective coordination of $LiClO_4$ to the ionophilic P2VP block.[48] A similar cause can be found in the inset TEM image for 240 °C, where the cylinders of the dark P2VP-rich phase are less organized in the bright PS matrix. Apart from the discontinuous decrease in *d*-spacing at OOT due to the mismatch between two microdomains, the increase in *d*-spacing in each microdomain with increasing temperature leads to speculation that in this LAM-to-HEX regime of high ion salt concentration, a weakening of the coordinative interaction with $LiClO_4$

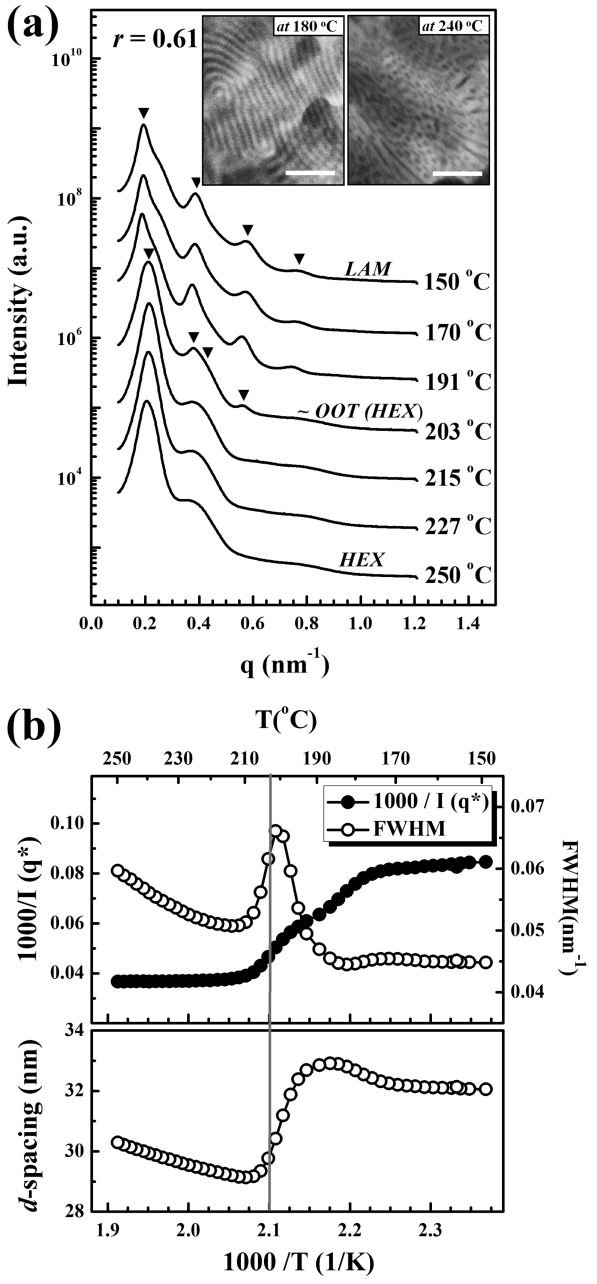

Figure 4. (a) SAXS intensity profiles for PS-*b*-P2VP-30 at $r = 0.61$ as a function of the scattering vector (q). All the profiles were measured at various temperatures during heating at a rate of 1 °C/min from 150 to 250 °C. The intensity profiles are vertically shifted by a factor of 5 for clarity. The TEM images in inset were obtained by quenching the sample at 180 and 240 °C, indicating LAM and HEX microdomains, respectively. The scale bar indicates 100 nm. (b) The inverse of the maximum intensity ($1/I(q^*)$), full-width at half-maximum (fwhm), and d-spacing ($d = 2\pi/q^*$) as a function of inverse temperature (1/K).

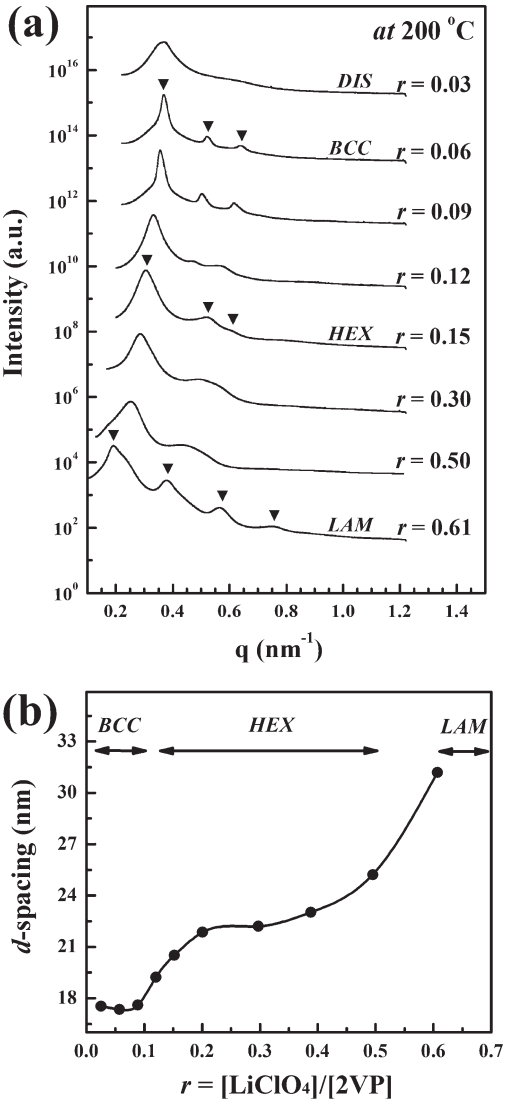

Figure 5. (a) SAXS intensity profiles for PS-*b*-P2VP-30 by varying from $r = 0.03$ to 0.61, which were measured at a constant temperature of 200 °C. The intensity profiles are vertically shifted by a factor of 10 for clarity. The morphologies are indicated with the characteristic peak points. (b) d-spacing ($d = 2\pi/q^*$) at 200 °C as a function of $r = [LiClO_4]/[2VP]$.

prevails over a decrease in χ between two block components in terms of a volumetric change.

All the SAXS profiles for $LiClO_4$-doped PS-*b*-P2VP-30 at $r = 0.03$ to 0.61, measured at a constant temperature of 200 °C, are displayed in Figure 5a. These profiles show ion salt concentration dependence on phase behavior. Incorporation of small amounts of $LiClO_4$ into disordered PS-*b*-P2VP-30, as shown in Figure 5a for $r = 0.03$, results in no change and the system remains disordered. Increasing molar ratio of $LiClO_4$ to $r = 0.12$ leads to BCC microdomains, while HEX microdomains appear at $0.15 \leq r \leq 0.50$. Further increasing molar ratio of $LiClO_4$ up to $r = 0.61$ leads to LAM microdomains eventually. A noteworthy feature is that the weight fraction of PS block decreases to 0.770 (−8%) from 0.844, as listed in Table 1. According to a general phase diagram of BCP melts (χN as a function of the volume fraction of one component), the increase in r from 0.03 to 0.61 should involve three phase boundaries at DIS-BCC, BCC-HEX, and HEX-LAM. It is therefore concluded that increasing amount of $LiClO_4$ results in a significant volumetric increase in the ionophilic P2VP block component. In particular, the primary peak at q^* moves toward lower q (or d-spacing increases) as the amount of $LiClO_4$ increases, as shown in Figure 5b. The shifts in d-spacing are perceptibly seen at both BCC-HEX and HEX-LAM transitions, as a consequence of the conformational changes in the polymer

dx.doi.org/10.1021/ma200429v |*Macromolecules* 2011, 44, 6085–6093

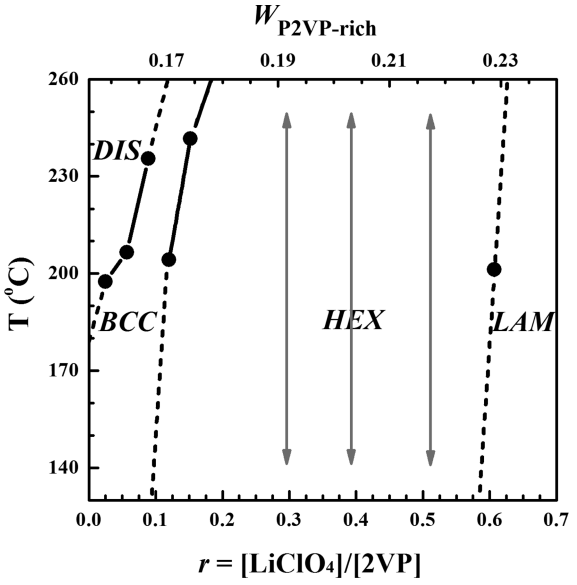

Figure 6. Phase diagram of $LiClO_4$-doped PS-*b*-P2VP-30 as a function of $r = [LiClO_4]/[2VP]$. All phase transition temperatures measured as ODT and OOT are indicated with the data points where phase boundaries are guided with dashed lines above the glass transition temperatures of PS and P2VP. A wide range of HEX microdomain was observed at $r = 0.30$, 0.39, and 0.51, as indicated with double headed arrows. $W_{P2VP\text{-}rich}$ indicates the weight fraction of P2VP-rich phase.

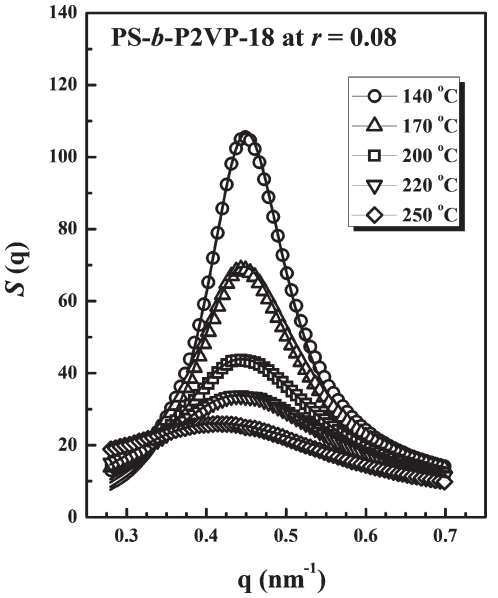

Figure 7. Structure factor (S) profiles for PS-*b*-P2VP-18 at $r = 0.08$. All the profiles were measured at various temperatures during heating from 140 to 250 °C. The solid lines are obtained by Leibler fittings.

chains due to the thermodynamic balance between the domain free energy and interfacial energy of two block components. A drastic increase in *d*-spacing from BCC to LAM microdomains (~80%) also reflects an effective volumetric change, which is presumably caused by a significant increase in interchain distance and chain stretching due to the selective coordination of $LiClO_4$ to the ionophilic P2VP block. It should be mentioned that a thermal scan by differential scanning calorimetry (DSC) indicates no crystallization effect in $LiClO_4$-doped PS-*b*-P2VP-30 up to $r = 0.61$.

The phase diagram of $LiClO_4$-doped PS-*b*-P2VP-30 is shown in Figure 6 as a function of $r = [LiClO_4]/[2VP]$. All phase transition temperatures measured as ODTs and OOTs are indicated with data points, where phase boundaries are guided with lines above the glass transition temperatures of PS and P2VP. Along with ion salt concentration dependence of the phase behavior in Figure 5, HEX microdomains were observed over a wide range of $r = 0.30$, 0.39, and 0.51, as indicated with double-headed arrows. In this temperature window a variety of morphological transitions such as DIS-BCC-HEX-LAM transitions are expected with increasing *r*, in parallel with the weight fraction of the P2VP-rich phase (indicated $W_{P2VP\text{-}rich}$ as on the top *x*-axis). HEX-LAM transitions at $r = 0.61$ represents that the composition is approaching to near symmetric volume since LAM microdomains were observed at $T < 203$ °C.

The effective interaction parameter (χ_{eff}) between two block components was evaluated to understand ion salt concentration and temperature dependence on χ_{eff} for $LiClO_4$-doped PS-*b*-P2VP. A low molecular weight PS-*b*-P2VP-18 ($M_n = 17500$ g/mol, $f_{PS} = 0.862$) was used to facilitate χ_{eff} evaluation over a wide range of disordered state. The absolute intensity was calibrated with a polyethylene standard.[49] We applied the absolute intensity ($d\Sigma/d\Omega$; cm^{-1}) of the samples to a dimensionless S using the following expression:

$$\left(\frac{d\Sigma}{d\Omega}\right)_{sample}(q) = \frac{KV_{ref}}{N_A}(a_1 - a_2)^2 S(q) \quad (1)$$

where K and N_A are a machine constant and Avogadro's number, respectively. V_{ref} is a reference molar volume by $V_{ref} = (\nu_{sp,i}[M]_{o,i} \times \nu_{sp,j}[M]_{o,j})^{1/2}$ with ν_{sp} and $[M]_o$ being temperature-dependent polymer specific volume (cm^3/g) and monomer molecular weight of component *i*, respectively. A contrast factor, a_i, can be calculated by

$$a_i = \frac{N_A \rho_i Z_{e,i}}{[M]_{0,i}} r_e \quad (2)$$

where ρ_i, $Z_{e,i}$, and r_e are the density of homopolymer *i*, total electron number, and the radius of an electron (2.82×10^{-13}cm), respectively.[49,50] The structure factor (S) profiles for PS-*b*-P2VP-18 at $r = 0.08$ were evaluated at various temperatures during heating from 140 to 250 °C, as plotted in Figure 7 as a function of the scattering vector (q). Similar to the SAXS intensity profiles for PS-*b*-P2VP-30 in Figure 1, a broad maximum near $q^* = 0.449$ nm^{-1} at 140 °C weakens and broadens as temperature increases, indicating a disordered state over temperature regime investigated. To extract χ_{eff}, we used Leibler theory based on the incompressible random phase approximation (RPA), as follows.[37]

$$S(q)^{-1} = \frac{F(x,f)}{N} - 2\chi \quad (3)$$

Here $x = R_g^2 q^2$, f is the volume fraction of one component, and N is the overall number of segments. We define $N = (V_i + V_j)/V_{ref}$, where V_i and V_{ref} are the molar volume of components and a reference molar volume, respectively. It should be pointed out that the effect of $LiClO_4$ was considered as a fractional factor into P2VP block in the reference molar volume and the contrast factor because of the selective coordination of $LiClO_4$ to the ionophilic

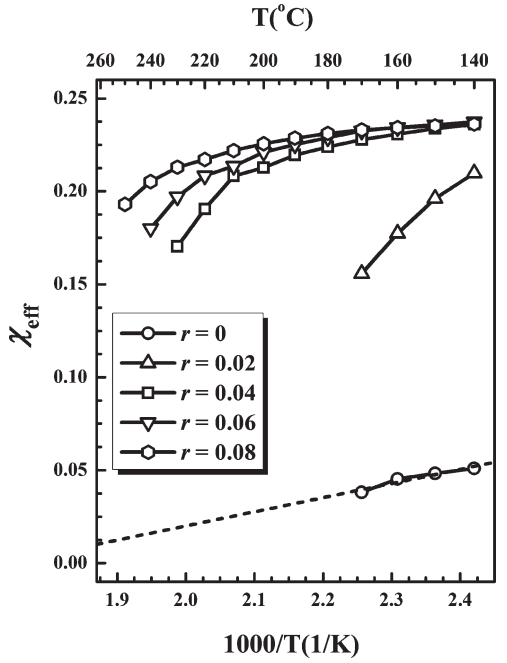

Figure 8. χ_{eff} for $LiClO_4$-doped PS-*b*-P2VP-18 as a function of inverse temperature (1/K) by varying from $r = 0$ to 0.08. A least-squares fit to the data for PS-*b*-P2VP-18 itself gives $\chi_{eff} = -0.1322 + 0.0761/T$.

P2VP block, rather than PS block. $F(x,f)$ can be obtained by

$$F(x,f) = \frac{g(1,x)}{g(f,x)g(1-f,x) - \frac{1}{4}[g(1,x) - g(f,x) - g(1-f,x)]^2} \quad (4)$$

where $g(f,x)$ is the Debye function defined by $g(f,x) = 2[fx + \exp(-fx) - 1]/x^2$. We varied f_{PS} from 0.862 to 0.858 when r increases to 0.08. Hence, the qualitative features of this analysis can provide useful insights for interactions between two block components. Adjusting χ_{eff} to the S profiles at each temperature produced the solid lines plotted in Figure 7, which fit well with the data and conform to eq 3.

Figure 8 shows χ_{eff} for $LiClO_4$-doped PS-*b*-P2VP-18 as a function of inverse temperature (1/K) by varying r from 0 to 0.08. A least-squares fit to the data for PS-*b*-P2VP-18 itself gives $\chi_{eff} = -0.1322 + 0.0761/T$, where the first and second terms represent the entropic and enthalpic contribution to χ_{eff}, respectively. The temperature dependence on χ_{eff} represents a qualitative ODT-type nature, where χ_{eff} eventually decreases as temperature increases. It deserves special emphasis that the incorporation of $LiClO_4$ into an asymmetric, disordered PS-*b*-P2VP-18 to $r = 0.08$ causes a huge increase in χ_{eff} between two block components from 0.051 to 0.247 (particularly at a constant temperature of 140 °C). On the basis of the SAXS measurements and TEM images, we conclude that the selective coordination of $LiClO_4$ to the ionophilic P2VP block results in a remarkable increase in χ_{eff} between two block components as well as a volumetric change with increasing r, leading to a variety of morphological transitions such as DIS-BCC-HEX-LAM transitions for $LiClO_4$-doped PS-*b*-P2VP-30.

We further focused on the ionic conductivity (σ) for $LiClO_4$-doped PS-*b*-P2VP-30 in order to elucidate the morphological effects, since incorporation of $LiClO_4$ into PS-*b*-P2VP-30 produced a variety of microphases. Especially in the samples displaying ODTs and OOTs, it is possible to compare the ionic conductivity depending on the morphologies at the same ion salt concentration when the samples were immediately quenched in liquid nitrogen (−196 °C) from above and below the transition temperatures. Figure 9 shows the ionic conductivity (σ) for $LiClO_4$-doped PS-*b*-P2VP-30 as a function of molar ratio (r), measured at 25 °C which is still below the glass transition temperatures of PS (100 °C) and P2VP (107 °C) for all samples. With increasing amount of $LiClO_4$, an initial rapid increase in σ to $r = 0.06$ can be attributed primarily to the increased number of charge carriers. However, a gradual increase in σ with further increasing amount of $LiClO_4$ indicates that this effect is noticeably retarded due to the restricted chain mobility by the selective coordination of $LiClO_4$ to the ionophilic P2VP block. However, any distinguishable step-variation in σ was not detected between DIS-BCC ($r = 0.06$), BCC-HEX ($r = 0.12$), and HEX-LAM ($r = 0.61$) morphologies for $LiClO_4$-doped PS-*b*-P2VP-30 in this study, indicating a morphology-independence on the ionic conductivity. This feature in the ionic conductivity may be in agreement with that observed for LiTFSI-doped PS-*b*-PEO,[39] even though it was measured within a limited temperature range to preserve the structural morphologies.

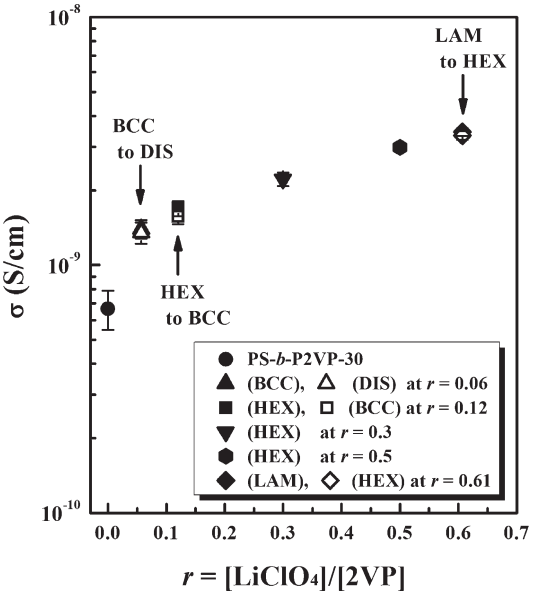

Figure 9. Ionic conductivity (σ) for $LiClO_4$-doped PS-*b*-P2VP-30 at r = 0, 0.06, 0.12, 0.3, 0.5 and 0.61, as a function of $r = [LiClO_4]/[2VP]$, which was measured at 25 °C. The samples displaying OOTs at $r = 0.06$, 0.12, and 0.61 were immediately quenched in liquid nitrogen (−196 °C) from above and below the transition temperatures (after annealing at 170 and 230 °C), and the samples with HEX morphology at $r = 0.3$ and 0.5 were quenched from 170 °C.

CONCLUSIONS

We extensively studied the phase transitions of $LiClO_4$-doped PS-*b*-P2VP as a function of temperature and ion salt concentration. For an asymmetric, disordered PS-*b*-P2VP-30, incorporation of $LiClO_4$ produced temperature-dependent ODTs and OOTs from spherical to lamellar microphases when ion salt concentration was adjusted. Ion salt concentration dependence on phase behavior at 200 °C resulted in BCC microdomains to

r = 0.09, HEX microdomains at 0.15 ≤ r ≤ 0.50, and LAM microdomains up to r = 0.61, while the weight fraction of PS block decreased to 0.770 (−8%) from 0.844. For $LiClO_4$-doped PS-*b*-P2VP-18 particularly in its disordered state, the structure factor (S) profiles were evaluated to extract the effective interaction parameter (χ_{eff}) between two block components, using Leibler theory based on the incompressible random phase approximation (RPA). On the basis of these results, we conclude that with increasing quantities of $LiClO_4$ a remarkable increase in χ_{eff} along with a volumetric change produced by the selective coordination of $LiClO_4$ to the ionophilic P2VP block led to morphological transitions of DIS-BCC-HEX-LAM structures. Furthermore, we also demonstrate that the ionic conductivity in the samples quenched from the different structures is morphology-independent, while it increases with increasing ion salt concentration.

■ ASSOCIATED CONTENT

Supporting Information. Depolarized light scattering measurements. This material is available free of charge via the Internet at http://pubs.acs.org.

■ AUTHOR INFORMATION

Corresponding Author
*E-mail: dyryu@yonsei.ac.kr.

■ ACKNOWLEDGMENT

This work was supported by the NRF grant (2010-0015410), Converging Research Center Program (2010K001430), and APCPI ERC program (R11-2007-050-00000), which are funded by the Ministry of Education, Science & Technology (MEST), Korea.

■ REFERENCES

(1) Elabd, Y. A.; Napadensky, E.; Walker, C. W.; Winey, K. I. *Macromolecules* **2006**, *39* (1), 399–407.
(2) Cho, B. K.; Jain, A.; Gruner, S. M.; Wiesner, U. *Science* **2004**, *305*, 1598–1601.
(3) Epps, T. H.; Bailey, T. S.; Pham, H. D.; Bates, F. S. *Chem. Mater.* **2002**, *14* (4), 1706–1714.
(4) Epps, T. H.; Bailey, T. S.; Waletzko, R.; Bates, F. S. *Macromolecules* **2003**, *36* (8), 2873–2881.
(5) Gomez, E. D.; Panday, A.; Feng, E. H.; Chen, V.; Stone, G. M.; Minor, A. M.; Kisielowski, C.; Downing, K. H.; Borodin, O.; Smith, G. D.; Balsara, N. P. *Nano Lett.* **2009**, *9* (3), 1212–1216.
(6) Majewski, P. W.; Gopinadhan, M.; Jang, W.-S.; Lutkenhaus, J. L.; Osuji, C. O. *J. Am. Chem. Soc.* **2010**, *132* (49), 17516–17522.
(7) Niitani, T.; Shimada, M.; Kawamura, K.; Kanamura, K. *J. Power Sources* **2005**, *146* (1−2), 386–390.
(8) Pan, J. H.; Zhao, X. S.; Lee, W. I. *Chem. Eng. J.* **2011**in press.
(9) Park, M. J.; Balsara, N. P. *Macromolecules* **2008**, *41* (10), 3678–3687.
(10) Patil, A.; Patil, V.; Wook Shin, D.; Choi, J.-W.; Paik, D.-S.; Yoon, S.-J. *Mater. Res. Bull.* **2008**, *43* (8−9), 1913–1942.
(11) Agrawal, R C.; G., P. P. *J. Phys. D: Appl. Phys.* **2008**, *41*, 223001.
(12) Singh, M.; Odusanya, O.; Wilmes, G. M.; Eitouni, H. B.; Gomez, E. D.; Patel, A. J.; Chen, V. L.; Park, M. J.; Fragouli, P.; Iatrou, H.; Hadjichristidis, N.; Cookson, D.; Balsara, N. P. *Macromolecules* **2007**, *40* (13), 4578–4585.
(13) Ruzette, A.-V. G.; Soo, P. P.; Sadoway, D. R.; Mayes, A. M. *J. Electrochem. Soc.* **2001**, *148* (6), A537–A543.
(14) Ioannou, E. F.; Mountrichas, G.; Pispas, S.; Kamitsos, E. I.; Floudas, G. *Macromolecules* **2008**, *41* (16), 6183–6190.
(15) Soo, P. P.; Huang, B.; Jang, Y.-I.; Chiang, Y.-M.; Sadoway, D. R.; Mayes, A. M. *J. Electrochem. Soc.* **1999**, *146* (1), 32–37.
(16) Stergiopoulos, T.; Arabatzis, I. M.; Katsaros, G.; Falaras, P. *Nano Lett.* **2002**, *2* (11), 1259–1261.
(17) Tarascon, J. M.; Armand, M. *Nature* **2001**, *414* (6861), 359–367.
(18) Trapa, P. E.; Huang, B.; Won, Y.-Y.; Sadoway, D. R.; Mayes, A. M. *Electrochem. Solid-State Lett.* **2002**, *5* (5), A85–A88.
(19) Li, J.; Khan, I. M. *Macromolecules* **1993**, *26* (17), 4544–4550.
(20) Li, J.; Mintz, E. A.; Khan, I. M. *Chem. Mater.* **1992**, *4* (6), 1131–1134.
(21) Bronstein, L. M.; Karlinsey, R. L.; Yi, Z.; Carini, J.; Werner-Zwanziger, U.; Konarev, P. V.; Svergun, D. I.; Sanchez, A.; Khan, S. *Chem. Mater.* **2007**, *19* (25), 6258–6265.
(22) Chiu, C.-Y.; Hsu, W.-H.; Yen, Y.-J.; Kuo, S.-W.; Chang, F.-C. *Macromolecules* **2005**, *38* (15), 6640–6647.
(23) Higa, M.; Fujino, Y.; Koumoto, T.; Kitani, R.; Egashira, S. *Electrochim. Acta* **2005**, *50* (19), 3832–3837.
(24) Kosonen, H.; Valkama, S.; Hartikainen, J.; Eerikainen, H.; Torkkeli, M.; Jokela, K.; Serimaa, R.; Sundholm, F.; ten Brinke, G.; Ikkala, O. *Macromolecules* **2002**, *35* (27), 10149–10154.
(25) Li, J.; Kamata, K.; Komura, M.; Yamada, T.; Yoshida, H.; Iyoda, T. *Macromolecules* **2007**, *40* (23), 8125–8128.
(26) Sang-Woog Ryu, P. E. T.; Olugebefola, S. C.; Gonzalez-Leon, J. A.; Sadoway, D. R.; Mayes, A. M. *J. Electrochem. Soc.* **2005**, *152*, A158–A163.
(27) Simone, P. M.; Lodge, T. P. *ACS Appl. Mater. Interfaces* **2009**, *1* (12), 2812–2820.
(28) Hamley, I. W.; Koppi, K. A.; Rosedale, J. H.; Bates, F. S.; Almdal, K.; Mortensen, K. *Macromolecules* **1993**, *26* (22), 5959–5970.
(29) Khandpur, A. K.; Foerster, S.; Bates, F. S.; Hamley, I. W.; Ryan, A. J.; Bras, W.; Almdal, K.; Mortensen, K. *Macromolecules* **1995**, *28* (26), 8796–8806.
(30) Matsen, M. W.; Bates, F. S. *J. Chem. Phys.* **1997**, *106* (6), 2436–2448.
(31) Foerster, S.; Khandpur, A. K.; Zhao, J.; Bates, F. S.; Hamley, I. W.; Ryan, A. J.; Bras, W. *Macromolecules* **1994**, *27* (23), 6922–6935.
(32) Matsen, M. W.; Bates, F. S. *Macromolecules* **1996**, *29* (4), 1091–1098.
(33) Bates, F. S.; Fredrickson, G. H. *Annu. Rev. Phys. Chem.* **1990**, *41*, 525–557.
(34) Floudas, G.; Vazaiou, B.; Schipper, F.; Ulrich, R.; Wiesner, U.; Iatrou, H.; Hadjichristidis, N. *Macromolecules* **2001**, *34* (9), 2947–2957.
(35) Hamley, I. W.; Castelletto, V. *Prog. Polym. Sci.* **2004**, *29* (9), 909–948.
(36) Hashimoto, T., *Thermoplastic Elastomers*; Hanser: New York, 1987.
(37) Leibler, L. *Macromolecules* **1980**, *13* (6), 1602–1617.
(38) Matsen, M. W.; Schick, M. *Phys. Rev. Lett.* **1994**, *72*, 2660.
(39) Wanakule, N. S.; Panday, A.; Mullin, S. A.; Gann, E.; Hexemer, A.; Balsara, N. P. *Macromolecules* **2009**, *42* (15), 5642–5651.
(40) Wanakule, N. S.; Virgili, J. M.; Teran, A. A.; Wang, Z.-G.; Balsara, N. P. *Macromolecules* **2010**, *43* (19), 8282–8289.
(41) Young, W.-S.; Epps, T. H. *Macromolecules* **2009**, *42* (7), 2672–2678.
(42) Wang, J.-Y.; Chen, W.; Russell, T. P. *Macromolecules* **2008**, *41* (13), 4904–4907.
(43) Kim, B.; Ahn, H.; Kim, J. H.; Ryu, D. Y.; Kim, J. *Polymer* **2009**, *50* (15), 3822–3827.
(44) Virgili, J. M.; Hexemer, A.; Pople, J. A.; Balsara, N. P.; Segalman, R. A. *Macromolecules* **2009**, *42* (13), 4604–4613.
(45) Gwee, L.; Choi, J.-H.; Winey, K. I.; Elabd, Y. A. *Polymer 51* (23), 5516−5524.
(46) Peyser, P. *Polymer Handbook*, 3rd ed.; Brandrup, J., Immergut, E. H., Eds.; John Wiley and Sons: New York, 1989; p VI 209.
(47) Kim, J. K.; Lee, H. H.; Sakurai, S.; Aida, S.; Masamoto, J.; Nomura, S.; Kitagawa, Y.; Suda, Y. *Macromolecules* **1999**, *32* (20), 6707–6717.

(48) Atorngitjawat, P.; Runt, J. *J. Phys. Chem. B* **2007**, *111* (48), 13483–13490.
(49) Han, S. H.; Kon Kim, J. *React. Funct. Polym.* **2009**, *69* (7), 493–497.
(50) Zha, W.; Han, C. D.; Lee, D. H.; Han, S. H.; Kim, J. K.; Kang, J. H.; Park, C. *Macromolecules* **2007**, *40* (6), 2109–2119.